Fault Section Identification of the Power Cables in Urban Distribution Networks by Amplitude Differences Between the Zero-Sequence Currents and Those Flowing in Cable Sheaths and Armors

Nan Peng, *Member, IEEE*, Peng Zhang, *Graduate Student Member, IEEE*, Rui Liang, *Member, IEEE*, Zhengyi Zhang, Xinyu Liu, Hao Wang, Yang Zhao, Xiaofeng Ren, and Xiuru Wang

***Abstract*—The power supply reliability of the urban distribution networks is being challenged by cable faults. Owing to the complex factors, such as system neutral, fault condition, and DG integration, it is difficult to detect and locate the fault cable. In this paper, the equivalent circuit model of the distribution cable is firstly created by considering the multi-conductor couplings. The mathematical relation of the amplitude differences between zero-sequence currents and those flowing in cable sheaths and armors at the local end of the healthy and fault cables are then derived in theory. Finally, according to the network topology and measurement locations, a novel method for identifying the fault cable section is proposed by using the defined space-measurement matrix. The simulation model of a real urban distribution network is established in PSCAD/EMTDC. The effectiveness and robustness of the proposed method are validated. The results demonstrate that the method is barely affected by the neutral grounding mode, fault initial condition, and distributed generation (DG) penetration level.**

***Index Terms*—Urban distribution cable, grounding line current, zero-sequence current, fault identification.**

Manuscript received 20 May 2022; revised 29 September 2022; accepted 11 November 2022. Date of publication 15 November 2022; date of current version 21 June 2023. This work was supported in part by the National Natural Science Foundation of China under Grant 52077215, and in part by the Natural Science Foundation of Jiangsu Province under Grant BK20201348. Paper no. TSG-00727-2022. *(Corresponding author: Rui Liang.)*

Nan Peng, Peng Zhang, Zhengyi Zhang, Xinyu Liu, Hao Wang, and Yang Zhao are with the School of Electrical Engineering, China University of Mining and Technology, Xuzhou 221116, China (e-mail: pncumt@163.com; zhangpeng20@cumt.edu.cn; TS21130093A31LD@cumt.edu.cn; 17175325@cumt.edu.cn; wh419194248@163.com; 17184994@cumt.edu.cn).

Rui Liang is with the School of Electrical Engineering, China University of Mining and Technology, Xuzhou 221116, China, and also with the School of Automation, Huaiyin Institute of Technology, Huaian 223003, China (e-mail: liangrui@cumt.edu.cn).

Xiaofeng Ren is with the Party Committee, State Grid Xuzhou Power Supply Company, Xuzhou 221005, China (e-mail: rxf_001@sina.com).

Xiuru Wang is with the Department of Science, Technology and Internet, State Grid Suqian Power Supply Company, Suqian 223800, China (e-mail: 741513796@qq.com).

Color versions of one or more figures in this article are available at https://doi.org/10.1109/TSG.2022.3222209.

Digital Object Identifier 10.1109/TSG.2022.3222209

I. Introduction

With the advances of urban distribution networks, a large number of power cables have been laid underground [1].

Due to the poor working environment, such as moisture, contamination, and internal defects, the distribution cables are prone to faults. However, finding a fault in the underground cable is difficult due to the inconvenient line inspection. Fast and reliable fault detection and location of the distribution cable is of great significance to improving the efficiency of repairment work and ensuring the reliability of power supply.

When a fault occurs in the distribution network, the voltages and currents deviate from the normal ones, providing the basis for fault detection. The three-phase and zero-sequence voltages of the main bus at the substation are commonly used to identify the faults. Since the voltages vary significantly prior to and after the faults, all types of the faults can be detected by setting appropriate thresholds of the monitored voltages. However, such fault detection method is susceptible to fault initial conditions, power disturbances, or some other factors.

After a fault is detected, it is necessary to identify the fault line section. The algorithms for fault section identification are generally divided into three main types: the impedance-based methods, transient signal- based methods, and artificial intelligent-based methods.

In the steady-state algorithms, the amplitudes and phases of the electrical signals are generally employed to identify the fault section [2]. The algorithm in [3] calculates the voltage deviation of each candidate line to identify the fault section. The voltage displacement of the neutral point is used to identify the fault section in [4]. By using the voltage phasors at each bus, a data bank is constructed to locate the fault section [5]. The steady-state methods have the advantages of easy implementation and low cost [6], but the reliability is easily affected by system parameter change and fault initial condition.

The transient signals related to the fault location is generated when a fault occurs in power distribution networks [7]. Compared with the steady-state methods, the transient

signal-based ones, widely adopted in the actual field, are not impacted by the neutral grounding mode and fault initial conditions. As for the transient signals-based methods, they can be further divided into two types: traveling waves based and non-traveling waves based methods, according to the transient signal type.

As for the non-traveling waves based methods, the fault section can be located based on the transient voltage difference [8], voltage or current energy [9], and zero-sequence current [10], [11], [12]. As for the traveling waves based methods, one of the most effective transient-state fault location algorithms, have been extensively applied [13]. By determining the arrival time of the traveling wave signals, an identification matrix is built in [14]. The graph theory is adopted in [15] to locate the fault section based on the traveling waves generated by the circuit breaker actions. The application of the traveling wave methods in the distribution networks is limited due to the high cost. In addition, the location results are not as good as those in transmission lines since the reflection and refraction of the traveling waves in the distribution network are more complicated [16].

With the fast development of artificial intelligence, the artificial intelligent-based algorithms have been gradually applied to fault location in power distribution lines. In [17], the wavelet energy spectrum entropy was employed to extract the fault features and establish the artificial neural network to identify the fault section of a power distribution network. The time-frequency features of the transient zero-sequence current signals is trained by the convolutional neural network to identify the fault line in [18]. To locate the fault section of the distribution network, the method in [19] used a one-dimension convolutional neural network to train the features of characterized zero-sequence current waveforms. The artificial intelligent-based methods have shown good performance in extracting the complex fault features. However, large amount of data and time-consuming training limit the application of these methods.

To automatically locate the fault section, many smart devices, such as the fault indicators [20], feeder terminal units [21], and μPMUs [22], [23], have been widely adopted in power distribution networks. The data from smart meters and fault indicators are jointly used for fault location in [24]. The method in [25] extracts the information of the smart meters and uses the fuzzy petri net to locate the fault section. However, the current smart units can be only applied to the severe faults and the complex faults cannot be identified by these units.

The underground cables in urban distribution networks have a complex structure where the significant electromagnetic couplings exist in the multiple conductors of the cables. The electrical model of the distribution three-core cable built in [26] does not consider the cable armor which commonly connects with the metallic sheath at terminals. Thus, the grounding line currents flow through the armors are also neglected in the analysis.

The topology of the urban distribution network is complex with many short cable feeders and branches. The fault conditions of the distribution cable are also complicated with different fault types, fault resistances and DG penetration levels. Most of the fault section identification methods are not applicable to such complex scenarios. Additionally, the three-phase voltages or currents cannot be easily measured in the distribution cables due to the special structure of the cable terminals. The accuracy and reliability of the fault section identification of the current methods cannot be guaranteed with low sampling rate and synchronous errors.

To address the above problems, this paper proposes a novel method for identifying the fault cable section in urban distribution network. The method uses the grounding line current and zero-sequence currents which can be measured at the local ends of the distribution cables. The method is verified by various simulations to be effective with different neutral grounding modes, fault conditions, and DG penetration. The main contributions of this paper are expressed as follows:

(1) The electrical model of the distribution three-core cable usually does not consider the cable armor which commonly connects with the metallic sheath at terminals. In this paper, an equivalent circuit model considering multiple conductors including the three-phase core conductors, sheath, and armor of the real three-core armored distribution cable is created in different conditions. The electromagnetic couplings among the cable conductors is considered by using the electrical parameters of the cable.

(2) The relationship between grounding line currents and zero-sequence ones of the distribution three-core cable is unclear. In this paper, the mathematical relation of the amplitude differences between the grounding line currents and zero-sequence ones of the healthy and fault cables are derived in theory. In detail, the amplitude difference between the grounding line and zero-sequence currents at the local end of the fault cable is larger than that of the healthy cable, which is the theoretical basis of the proposed fault section identification method.

(3) Most of the fault section identification methods are not applicable to the complex scenarios, such as intermittent faults and unbalanced loads and laterals. And the accuracy and reliability of the fault section identification of the current methods cannot be guaranteed with low sampling rate and synchronous errors. Compared with the current methods, the advantages of the proposed method in this paper include convenient measurement, low sampling rate, no need for synchronization or the prior knowledge, and short computation time. The proposed method is effective in both the permanent and the intermittent arc faults. It is not affected by unbalanced loads and different laterals.

II. Fault Section Location Method for Three-Core Distribution Cables

A. Equivalent Circuit Model of the Three-Core Distribution Cable Considering Conductor Coupling

As for a three-core distribution cable, the three-phase conductors together with the metallic sheath are arranged in an equilateral triangle. The mutual impedance between any two core-conductors are different from that between the core-conductor and sheath. Thus, the arrangement of the three-core

cable is not asymmetrical. The impedance and admittance matrices $\boldsymbol{Z}$ and $\boldsymbol{Y}$ of the three-core cable can be expressed by

$$\begin{cases} \boldsymbol{Z} = \begin{bmatrix} Z_{AA} & Z_{AB} & Z_{AC} & Z_{AS} & Z_{AM} \\ Z_{BA} & Z_{BB} & Z_{BC} & Z_{BS} & Z_{BM} \\ Z_{CA} & Z_{CB} & Z_{CC} & Z_{CS} & Z_{CM} \\ Z_{SA} & Z_{SB} & Z_{SC} & Z_{SS} & Z_{SM} \\ Z_{MA} & Z_{MB} & Z_{MC} & Z_{MS} & Z_{MM} \end{bmatrix} \\ \boldsymbol{Y} = \begin{bmatrix} Y_{AA} & Y_{AB} & Y_{AC} & Y_{AS} & Y_{AM} \\ Y_{BA} & Y_{BB} & Y_{BC} & Y_{BS} & Y_{BM} \\ Y_{CA} & Y_{CB} & Y_{CC} & Y_{CS} & Y_{CM} \\ Y_{SA} & Y_{SB} & Y_{SC} & Y_{SS} & Y_{SM} \\ Y_{MA} & Y_{MB} & Y_{MC} & Y_{MS} & Y_{MM} \end{bmatrix} \\ Z_{AA} = Z_{BB} = Z_{CC} = z_1, Y_{AA} = Y_{BB} = Y_{CC} = y_1 \\ Z_{AB} = Z_{BC} = Z_{CA} = z_2, Y_{AB} = Y_{BC} = Y_{CA} = y_2 = 0 \\ Z_{AS} = Z_{BS} = Z_{CS} = z_3, Y_{AS} = Y_{BS} = Y_{CS} = y_3 \\ Z_{AM} = Z_{BM} = Z_{CM} = z_4, Y_{AM} = Y_{BM} = Y_{CM} = y_4 = 0 \\ Z_{SS} = z_5, Y_{SS} = y_5, Z_{SM} = z_6, Y_{SM} = y_6 \\ Z_{MM} = z_7, Y_{MM} = y_7 \end{cases} \tag{1}$$

where Z_{PP} and Y_{PP} represent the self-impedance and self-admittance of the core conductor of phase P ($P \in \{\mathrm{A}, \mathrm{B}, \mathrm{C}\}$) in per unit length of the cable. Z_{SS} and Y_{SS} denote the self-impedance and self-admittance of the metallic sheath in per unit length of the cable. Z_{MM} and Y_{MM} denote the self-impedance and self-admittance of the armor in per unit length of the cable. Z_{PQ} and Y_{PQ} represent the mutual impedance and admittance between the core conductors of phases P and Q ($Q \in \{\mathrm{A}, \mathrm{B}, \mathrm{C}\}$) in per unit length of the cable. Z_{PS} and Y_{PS} denote the mutual impedance and admittance between the core conductor of phase P and metallic sheath in per unit length of the cable. Z_{PM} and Y_{PM} represent the mutual impedance and admittance between the core conductor of phase P and armor in per unit length of the cable. Z_{SM} and Y_{SM} are the mutual impedance and admittance between the metallic sheath and armor in per unit length of the cable.

Based on the finite element method, the mutual coupling capacitances and inductances of the three-core distribution cable can be computed. In theory, it takes total conductor current I as known and boundary condition to compute the current density J_s. Then the impedance matrix Z can be acquired by

$$J_s = \sigma Z I \tag{2}$$

where σ denote diagonal matrix of the conductor conductivity. According to the finite element analysis, any element $Y_{m,n}$ in admittance matrix Y can be computed by

$$Y_{m,n} = \sum_{i_m=1}^{n_m} K_{i_m.n} \tag{3}$$

where n_m denotes the total number of the discrete points on dielectric m surface, i_m denote the discrete point code, $K_{im,n}$ denote the element in matrix of the finite element coefficient.

Taking the three-core distribution cable (YJV22-6/10kV-3*70mm^2) as an example, the computed result of elements of the impedance matrix $\boldsymbol{Z}$ and admittance matrix $\boldsymbol{Y}$ in per unit length is

$$\begin{cases} z_1 = 3.61 * 10^{-4} + j1.41 * 10^{-3}\Omega\ /\mathrm{m}, y_1 = j3.90 * 10^{-8}\mathrm{S/m} \\ z_2 = 1.09 * 10^{-4} + j1.24 * 10^{-3}\Omega\ /\mathrm{m}, y_2 = 0 \\ z_3 = 3.77 * 10^{-5} + j4.38 * 10^{-4}\Omega\ /\mathrm{m}, y_3 = -j3.90 * 10^{-8}\mathrm{S/m} \\ z_4 = 7.97 * 10^{-5} + j9.38 * 10^{-4}\Omega\ /\mathrm{m}, y_4 = 0 \\ z_5 = 3.18 * 10^{-4} + j4.38 * 10^{-4}\Omega\ /\mathrm{m}, y_5 = j5.29 * 10^{-7}\mathrm{S/m} \\ z_6 = 2.66 * 10^{-5} + j3.13 * 10^{-4}\Omega\ /\mathrm{m}, y_6 = -j1.28 * 10^{-7}\mathrm{S/m} \\ z_7 = 5.80 * 10^{-4} + j8.37 * 10^{-4}\Omega\ /\mathrm{m}, y_7 = j2.80 * 10^{-6}\mathrm{S/m} \end{cases} \tag{4}$$

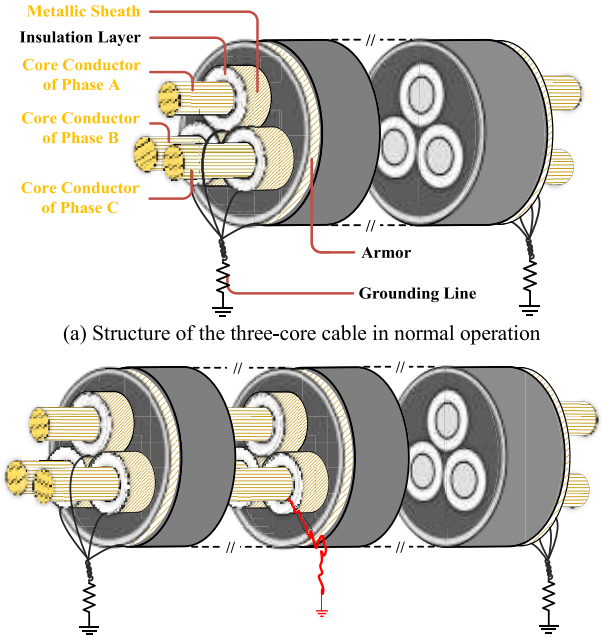

(a) Structure of the three-core cable in normal operation

(b) Structure of the three-core cable in fault condition

Fig. 1. Diagram of the three-core cable in normal and fault conditions.

The structures of the three-core cables in normal operation and fault condition are depicted in Fig. 1 (a) and Fig. 1 (b). Aiming at the three-core distribution cables in normal operation and fault condition, the equivalent circuit models considering the core conductors, metallic sheath and armor is constructed and displayed in Fig. 2. The electric and magnetic coupling among the core conductors, sheath and armor are characterized by the mutual admittances and impedances shown in (1). In Fig. 2(a), l is the total length of the cable. R_{SG} represents the resistance of the grounding line. Generally, the single-phase fault in the cable can be classified into two types: core-sheath fault and core grounding fault. When a single-phase fault occurs in the cable, the equivalent circuit model of the fault cable is illustrated in Fig. 2(b). The fault is x away from the local end of the cable. Most of the faults in cables are permanent faults, which means the fault resistance can be considered as constant. However, an arc fault may occur between the phase conductor and the metallic sheath of the cable. Thus, the fault is modeled as arc fault with non-linear resistance varying with time. $I_{fw}(t)(w \in \{1, 2, 3\})$ represents the arc current. t is the time variable. $R_{f1}(t)$, $R_{f2}(t)$ and $R_{f3}(t)$ are the fault resistances. As for the core-sheath fault, $R_{f2}(t)$ and $R_{f3}(t)$ don't exist. R_{f1}(t), $R_{f2}(t)$ and $R_{f3}(t)$ all exist in the core grounding fault. In Fig. 1, Y_{PPl}=0.5lY_{PP}, Z_{PPl}=lZ_{PP}, and

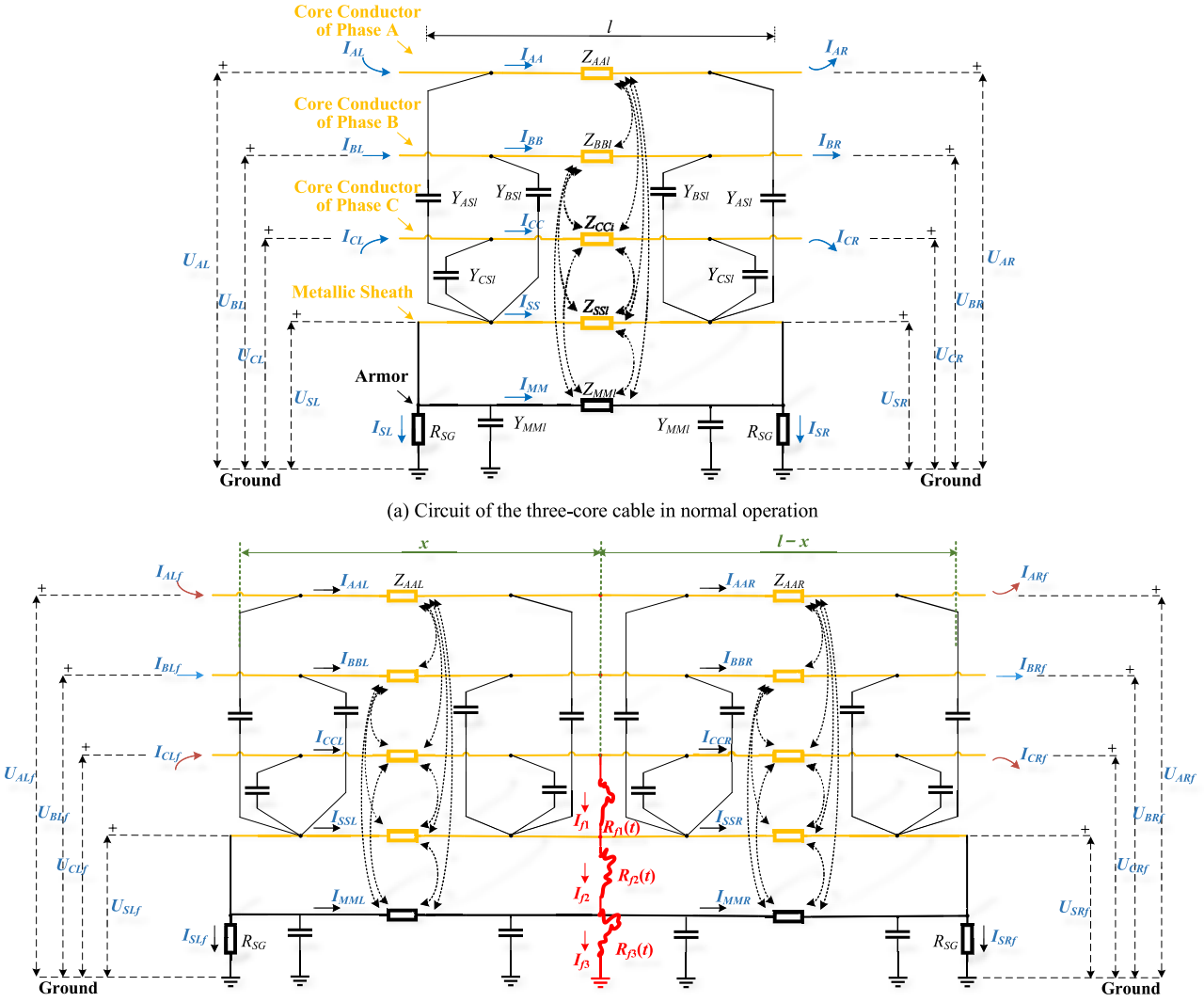

(a) Circuit of the three-core cable in normal operation

(b) Circuit of the three-core cable in fault condition

Fig. 2. Equivalent circuits of the three-core cables in normal operation and fault condition.

so on. In Fig. 2, we have Y_{PPL}=0.5xY_{PP}, Y_{PPR}=0.5$(l-x)Y_{PP}$, Z_{PPL}=xZ_{PP}, Z_{PPL}=$(l-x)Z_{PP}$, and so on.

The high-voltage cable (≥110kV) is usually multiple grounded for long transmission distance (≥10km). However, for the distribution cable, it does not have the multiple grounding bonding since the length of the cable section is commonly short (only about 100m∼500m). According to the operation standards for the power distribution cables in China (GB 50217–2018), the metallic sheath of the three-core distribution cable is only grounded at both ends (rather than along the cable) via the grounding lines in order to mitigate the bad impact of the electromotive force induced by the core conductors. Thus, there is no problem of the multiple grounding bonding effect on the grounding line current for the three-core distribution cables.

Compared with the transducers for measuring the three-phase currents or voltages, those for measuring the grounding line current are more easily installed at the local end of the three-core distribution cable [27]. The zero-sequence current can be measured by an ordinary zero-sequence current transformer in field. The zero-sequence current transformer is commonly toroidal or rectangular, with a hole to make the three-phase core conductors pass through.

It is convenient to install and dismantle the transducers in the cable. As shown in Fig. 3, the zero-sequence current of a three-core cable is measured at the terminal by the zero-sequence current transformer (ZCT) in the actual field. The metallic sheath and armor are stripped off at the terminal of the cable. Thus, the ZCT is set on the three-phase conductors only with insulation layers of the cable to directly measure the zero-sequence current of the three-core distribution cable. Thus, the summation of the three-phase currents, commonly used for the overhead transmission lines, is not needed for obtaining the zero-sequence of the distribution cable. Additionally, the metallic sheath and armor can only shield the electric field (affecting the voltage signal) but cannot shield the magnetic field (affecting the current signal). Thus, the shielding effect of the metallic sheath and armor (Faraday cage effect) has little effect on the measurement of the zero-sequence current.

The current transformer of the MV distribution network may be saturated when measuring the large fault current. However, as for the 10kV distribution network, the neutral point at main

Fig. 3. Measurement of the zero-sequence current in the actual field.

station are indirectly grounded (using a ground transformer). Most of the faults are not permanent short-circuit faults. Thus, the fault current is not as large as that in the high-voltage transmission network. In general, the zero-sequence current of a 10kV distribution network ranges from several amperes to dozens of amperes. The probability of current transformer saturation in the 10kV distribution network is low In addition, the main reason of saturation is that the signal transformer has the structure of iron core, which is common in the electromagnetic transformer. However, with the development of signal transducers, more and more current transformers have removed the structure of iron core, for example Rogowski's current coils and photoelectric transformers. In these transformers, there is no saturation effect.

B. Relationship Between Grounding Line Currents and Zero-Sequence Ones at the Local Ends of the Cables

A typical urban distribution cable network is displayed in Fig. 4. Based on the established equivalent circuit models of the three-core cable, the theoretical analysis on the relationship between grounding line currents and zero-sequence currents at the local ends of the cables is conducted. Details are as follows.

According to the analysis of the zero-sequence and grounding line current of the healthy cable k in Appendix A, we know that the size relation between I_{SLk} and I_{0Lk} is:

$$|I_{SLk}| < 3|I_{0Lk}| \tag{5}$$

According to (5), it is easy to know that $|I_{SLk}| - |I_{0Lk}| < 2|I_{0Lk}|$. Based on the analysis in Appendix B, the relationship between the grounding line current and zero-sequence current at the local end of the fault cable j can be expressed as

$$\left|I_{SLj}\right| \geq 3\left|I_{0Lj}\right| \tag{6}$$

where I_{0Lj} denotes the zero-sequence current at the local end of cable j. The detailed process of obtaining (6) is shown in Appendix B. It is clear from (6) that $|I_{SLj}| - |I_{0Lj}| \geq 2|I_{0Lj}|$.

For an ungrounded or small resistance grounded distribution network, I_{0Lj} is larger than I_{0Lk}. For an arc-suppression coil grounded network, the transient zero-sequence current is not affected by the compensatory inductive current. Additionally,

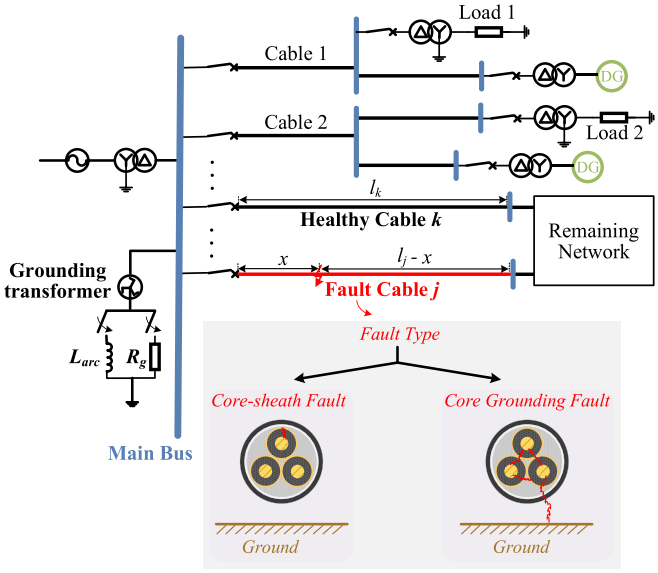

Fig. 4. Diagram of a typical urban distribution cable network.

as shown in Fig. 4, the winding type of the distribution transformer is Δ/Y, which means the power flows of distributed generator (DG) do not affect the zero-sequence and grounding line currents. In other words, the zero-sequence and grounding line currents with integration of DG is basically identical to those without DG. Thus, we have

$$\begin{cases} \Delta\ I_j > \Delta\ I_k \\ \Delta\ I_j = \left|I_{SLj}\right| - \left|I_{0Lj}\right|,\ \Delta\ I_k = |I_{SLk}| - |I_{0Lk}| \end{cases} \tag{7}$$

In (7), ΔI_j and ΔI_k represent the amplitude differences between the grounding line currents and zero-sequence currents at the local ends of cable j and k. Since the voltages of the healthy phases increase after a fault occurs in the distribution network with neutral point indirectly grounded, the charging current generated by the capacitances to ground of the cable grows a lot. The authors admit that fact. However, the charging current reaches the steady-state value after a rapid growth. In (7), the charging current is represented by the zero-sequence current and grounding line current since they are affected by the cable capacitances to ground. Equation (7) only shows the relationship between the steady-state zero-sequence current and grounding line one whose amplitudes have reached the steady-state stage. Thus, equation (7) does not show the increase stage of the charging current. On the contrary, it only shows the amplitude of the charging current when it reaches the steady state.

C. Fault Section Identification Algorithm

In an actual distribution cable network, there are many cable sections. To efficiently and automatically locate the fault section, a method considering the network topology and measurement locations is proposed as elaborated below.

As for a distribution cable network with N nodes and q sections, the space-measurement matrix $\boldsymbol{M}_{\mathrm{sm}}$ is defined as

$$\begin{cases} \boldsymbol{M}_{\mathrm{sm}} = \left[m_{gh}\right]_{N\times q} (1 \leq g \leq N, 1 \leq h \leq q) \\ m_{gh} = \begin{cases} 1, & h \text{ is located in the cable connected to } g \\ 0, & h \text{ is not located in the cable connected to } g \end{cases} \end{cases} \tag{8}$$

where m_{gh} is the element in the gth row and hth column of $\boldsymbol{M}_{\rm sm}$. The row and column of $\boldsymbol{M}_{\rm sm}$ represent the node and measurement point (cable section) numbers, which are fixed in the distribution network. It can be seen that the element in $\boldsymbol{M}_{\rm sm}$ depends on the space location determined by the node and measurement point. The measurement unit is mounted at the local end of each cable section to record the grounding line current and zero-sequence current.

After constructing the space-measurement matrix $\boldsymbol{M}_{\rm sm}$ of the distribution network, the grounding line current at the local end of the main cable feeder $i_{SL\_MF}(t)$ is acquired to identify the single-phase fault by

$$\max\left(\left|i_{SL\_MF}(t)\right|\right) > \zeta_{\max}, \left(t \geq t_0 + t_p\right) \tag{9}$$

where t represents the time variable. t_0 denotes the time corresponding to the singularity of $i_{SL\_MF}(t)$. t_p is the time interval corresponding to the power frequency. ζ_{max} is the maximum value of $i_{SL\_MF}(t)$ during the operation of the distribution cable network. If (9) is satisfied, a single-phase fault occurs in a cable section. The amplitude difference between the grounding line current and zero-sequence current at the local end of each cable section is then calculated. The amplitude difference ratio matrix $\boldsymbol{M}_r$ is created by

$$\begin{cases} \boldsymbol{M}_r = [m_{uv}]_{q\times q}(1 \leq u, v \leq q) \\ m_{uv} = \frac{d_u}{d_v}, d_u = \text{Max}(|i_{SLu}(t)|) - \text{Max}(|i_{0Lu}(t)|) \end{cases} \tag{10}$$

In (10), m_{uv} is the element in the uth row and vth column of $\boldsymbol{M}_r$. d_u and d_v represent the amplitude differences between the grounding line currents and zero-sequence currents of cable sections u and v,. Function Max ( ) is to obtain the maximum of the signal. The data window can be set as $[t_0,\ \ t_0 + 0.25t_p]$. Since the data window is very short, the amplitudes of the current signals are extracted before isolation of the fault cable section. Besides, locations of the measurement points are fixed and the topology of the distribution network remains unchanged during the fault section identification before the fault isolation. Thus, the matrix $\boldsymbol{M}_{\rm sm}$ does not change in the data window. The sum of the elements in the rows of $\boldsymbol{M}_r$ is denoted as $\boldsymbol{V}_s$:

$$\mathbf{V}_s = [v_u]_{q\times 1}(1 \leq u \leq q), v_u = \sum_{v=1}^{q} m_{uv} \tag{11}$$

In (11), v_u represents the uth element of $\boldsymbol{V}_s$. The number corresponding to the maximum element in $\boldsymbol{V}_s$ is written as $u_{\max}$. Finally, the numbers of the ends of the fault cable section can be determined by

$$\begin{cases} \boldsymbol{M}_{sm}(n_L, u_{\max}) = 1 \\ \boldsymbol{M}_{sm}(n_R, u_{\max}) = 1 \end{cases} \tag{12}$$

where n_L and n_R are the numbers of the local and remote ends of the fault cable section.

The proposed method to obtain current fault and the related section is based on the grounding line currents and zero-sequence currents at the local ends of cable sections in a distribution network. In detail, after numbering the cable section nodes and measurement units, the space-measurement matrix $\boldsymbol{M}_{\rm sm}$ can be constructed by (8). Then the method uses the criterion (9) to identify the single-phase fault. If it is satisfied, the time window of the sampled current signals needs to be set for construct $\boldsymbol{M}_r$, compute $\boldsymbol{V}_s$ by (10), (11). At last, the fault section can be obtained by (8) and (12). The steps for implementing the proposed method are shown in Fig. 5.

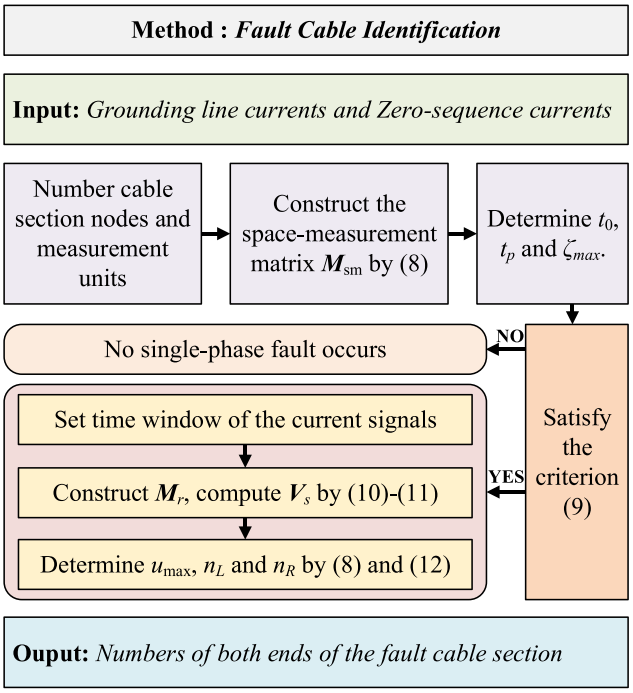

Fig. 5. Flowchart of the proposed fault sensing method.

Based on the proposed fault sensing method, the circuit breaker in the busbar cabinet and the ring network cabinet will cut the faulted feeder and the faulted cable section will be isolated by the load switch in the cable branch box. Then the non-fault area restores power supply for ensuring the reliability. After the operating personnel clear the fault, the whole distribution network returns to the normal operation.

The balanced fault in the overhead line does not produce the zero-sequence current. However, for the distribution three-core cables, the balanced faults (two-phase or three-phase short-circuit faults) will damage metallic sheath by the local high temperature (shown in Fig. 4). For the three-phase short circuit fault, the fault resistances between the three-phase conductors are different due to the nonlinearity and randomness of the fault arc. The probability of ideal balanced fault conditions in the distribution cable with a fault is very low. According to the operation standards for the power distribution cables in China (GB 50217–2018), the metallic sheath of the three-core distribution cable is only grounded at both ends via the grounding lines in order to mitigate the bad impact of the electromotive force induced by the core conductors. After the balanced fault occurs, the fault current will flow to the ground via the grounding line, which produces the unbalanced component. The zero- sequence current exist in all types of the faults in the distribution three-core cables. Thus, the proposed method dependent on the zero-sequence current, is still effective when the balanced fault occurs in the three-core distribution cable.

D. Deployment of the Measurement Units and Cost Analysis

To apply the proposed method, the zero-sequence current and groundling line current are acquired. In the actual field, the measurement unit can be placed at the cable terminal in the ring network unit, cable branch box, or outlet cabinet at the main station and switching station. The number of the measurements needed for implementing the proposed method depends on the scale of the distribution network and the requirement for fault section location. Under the highest standard for fault section identification, the method needs K zero-sequence currents and K grounding line currents measured at the local ends of these sections to identify the fault one if there are X cable branches with K line sections in the distribution network ($1 \leq X \leq K$). However, if there are H ($H<X$) cable branches with G ($G<K$) line sections whose lengths are around the shortest length (0.3km~0.5km) of the distribution cable segment, the method only needs $K-G$ zero-sequence currents and $K-G$ grounding line currents measured at the local ends of the $K-G$ line sections.

The cost of the measurement C_M for the method application can be estimated by

$$\begin{cases} C_M = C_T + C_S + C_C \\ C_T = C_{ZT} + C_{GT} \\ C_S = N_M C_{SE} \end{cases} \tag{13}$$

where C_T, C_S, and C_C represent the costs of transducers, signal sampling and data communication, respectively. C_T can be divided into two parts: the cost of zero-sequence transformers C_{ZT} and that of the grounding line current transformer C_{GT}. C_{SE} denotes the cost of a signal sampling unit. N_M is the number of the needed measurements. For current urban distribution networks, the zero-sequence current transformers are basically equipped in each line section, which means that C_{ZT} can be ignored. Thus, $C_T = C_{GT} \leq KC_{ct}$ where C_{ct} represents the cost of a current transformer. Since the proposed method does not require synchronization and high sampling rate (only 3.2kHz), cheap signal sampling units can be used and C_{SE} is low. For a signal sampling unit with two input signal channels, 8-bit AD, 3.2kHz sampling rate, 200MB RAM and 2G ROM, the price (C_{SE}) is about 70 dollars. Additionally, only the amplitude difference between the zero-sequence current and grounding line current at each measurement point is transmitted to the main station, indicating that C_C is low in the actual field. The price of a GPRS wireless communication module is only 5 dollars. According to the above analysis, we have $C_M \leq K$ ($C_{ct} + C_{SE} + C_C$). Taking the current transformer (whose type is LXK-10kV-120mm) as an example, the price (C_{ct}) is about 25 dollars. For a common distribution network, K usually varies from 50 to 100. Thus, the highest cost of the measurement for the method application is in the range of 5000 to 10000 dollars. However, the cost of the measurement of the current distribution automation system for fault section location in the actual field is far higher than 10000 dollars (usually exceeds 100000 dollars). In summary, the cost of implementing the proposed method is not high.

III. Theory Verification and Method Validation

To verify the theoretical analysis and validate the method, a simulation model based on a real 10kV urban distribution cable network is constructed by PSCAD/EMTDC. The diagram of the network is shown in Fig. 6. Switch K1 and K2 determine the neutral grounding mode of the network. TG represents neutral grounding transformer. The network contains six cable feeders. The first feeder includes many cable sections and branches. The black spots represent the branch nodes or cable ends. The main parameters of the simulated distribution cable network are shown in Table I.

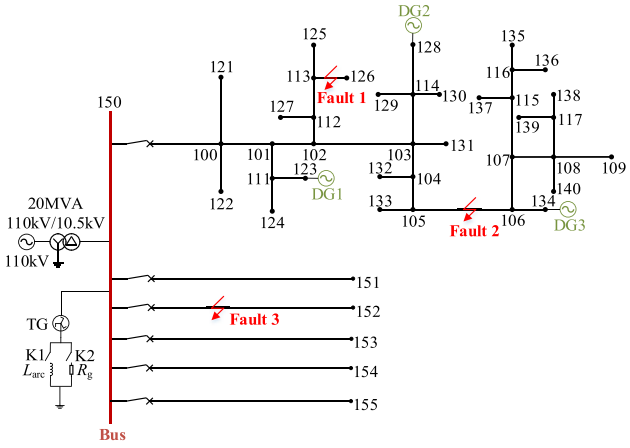

Fig. 6. Diagram of the simulated distribution cable network.

TABLE I
Main Parameters of the Simulated Distribution Cable Network

Rated Voltage(kV)	110
Main Transformer Capacity (MVA)	20
Ratio of the Main Transformer	110kV/10.5kV
Transformer Leakage Reactance (pu)	0.06
Type of the Cable	YJV22-6/10kV-3*70mm^2
Sampling Rate (kHz)	3.2
Resistance of the Grounding Line (Ω)	1
Overcompensation Degree of the Arc-suppression Coil (%)	8
Neutral Grounding Resistance R_g (Ω)	10
Penetration Level of DG1 (%)	15
Penetration Level of DG2 (%)	12
Penetration Level of DG3 (%)	12

Fig. 6 shows only one power transformer (110kV/10kV) at the main station. In the actual field, there are generally two redundant transformers at the upstream grid where both of them are contributed to the fault current. However, this contribution only occurs in the short-circuit fault (fault current path does not include the ground) of the overhead transmission line. As for the distribution cable network, the path of the fault current includes the ground. Since the type of the windings of the power transformer at the main station is Y/Δ (Δ winding can isolate the zero-sequence component), it does not contribute to the ground currents (including the zero-sequence current and grounding line current) of the distribution network after a fault occurs in the cable. Thus, even though there are two redundant transformers at the upstream grid, they don't contribute to the fault current of the distribution cable.

The actual cable section consists of several cable segments. For the 10kV distribution cable section, the length of

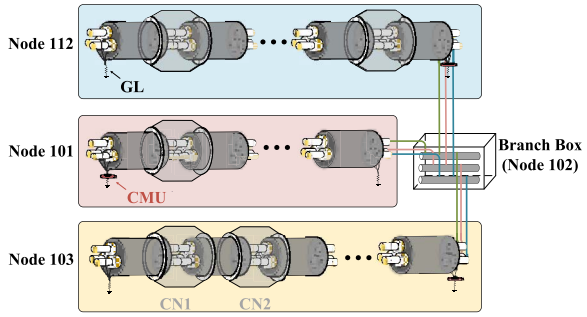

Fig. 7. Connection and measurement unit deployment of the cable sections.

TABLE II
CABLE LENGTH IN THE SIMULATION MODEL

N_L	N_R	L(km)	N_L	N_R	L(km)	N_L	N_R	L(km)
150	100	4.7	100	121	7.1	100	122	3.6
100	101	2.8	101	111	1.6	111	123	5.4
111	124	9.9	101	102	6.2	102	112	2.3
112	127	1.5	112	113	3.1	113	125	2.1
113	126	6.9	102	103	8.8	103	114	4.6
114	128	1.3	114	129	2.5	114	130	3.6
103	131	1.7	103	104	2.4	104	132	5.8
104	105	2.7	105	133	1.2	105	106	9.1
106	134	2.6	106	107	4.7	107	115	3.2
115	137	5.2	115	116	3.3	116	135	2.5
116	136	6.4	107	108	5.9	108	117	4.2
117	138	3.5	117	139	1.1	108	109	7.2
108	140	7.4	150	151	10.0	150	152	5.5
150	153	1.0	150	154	8.2	150	155	3.0

the cable segment is about 300m∼500m. Taking the cable sections (101-102, 102-112, and 102-103) as examples, the connection structures of these cable sections are illustrated in Fig. 7. GL represents the grounding line. CMU represents the current measurement unit for measuring the grounding line current. The zero-sequence current of a distribution cable can be directly measured by a zero-sequence transformer in actual field. CN1, CN2, ... denote the connection nodes of the cable section. The CMUs in simulation are deployed at the local ends of the distribution cables and the branch boxes.

The cable lengths, loads and numbers of the measurement units are listed in Table II, III and IV, respectively. 'N_L' and 'N_R' denote the local and remote node numbers of the cable sections. 'L' represents the cable section length. 'M_N' denotes the number of the measurement unit. Various fault simulations with different initial conditions are conducted. The results are shown and discussed below.

A. Case Study

Three faults cases are considered in this section. The information of the cases is listed in Table V. 'NG' represents the neutral grounding mode of the network. 'UNG', 'RG' and 'ASG' denote the ungrounded, small resistance grounded and arc-suppression coil grounded neutrals. 'FCS' denotes the fault cable section. 'R_F' represents the fault resistance. 'x_F' is the fault distance from the local end of the cable section. 'FT' denotes the fault type. 'CSF' and 'CGF' represent the core-sheath fault and core grounding fault. The zero-sequence currents and grounding line currents at the local ends of the

TABLE III
LOADS IN THE SIMULATION MODEL

Node	Load (per Phase)	Node	Load (per Phase)
121	0.25MW+j0.02MVar	122	0.27MW+j0.03MVar
124	0.26MW+0.04MVar	125	0.27MW+0.03MVar
126	0.28MW+0.02MVar	127	0.23MW+0.04MVar
129	0.29MW+0.02MVar	130	0.25MW+0.03Mvar
131	0.28MW+0.05Mvar	132	0.29MW+0.02MVar
133	0.26MW+0.03Mvar	135	0.3MW+0.04MVar
136	0.26MW+0.04MVar	137	0.24MW+0.02MVar
138	0.28MW+0.03Mvar	139	0.29MW+0.01MVar
140	0.24MW+0.05MVar	109	0.25MW+0.04MVar
151	0.23MW+0.02Mvar	152	0.28MW+0.04MVar
153	0.29MW+0.04MVar	154	0.25MW+0.05Mvar
155	0.24MW+0.01Mvar	---	---

TABLE IV
NUMBERS OF THE MEASUREMENT UNITS IN THE SIMULATION MODEL

N_L	N_R	M_N	N_L	N_R	M_N	N_L	N_R	M_N
150	100	1	100	121	2	100	122	3
100	101	4	101	111	5	111	123	6
111	124	7	101	102	8	102	112	9
112	127	10	112	113	11	113	125	12
113	126	13	102	103	14	103	114	15
114	128	16	114	129	17	114	130	18
103	131	19	103	104	20	104	132	21
104	105	22	105	133	23	105	106	24
106	134	25	106	107	26	107	115	27
115	137	28	115	116	29	116	135	30
116	136	31	107	108	32	108	117	33
117	138	34	117	139	35	108	109	36
108	140	37	150	151	38	150	152	39
150	153	40	150	154	41	150	155	42

TABLE V
INFORMATION OF THE FAULT CASES

Case	NG	FCS	R_F	FT	x_F
①	UNG	n_L=113, n_R=126	200Ω	CSF	2.9km
②	RG	n_L=105, n_R=106	500Ω	CSF	5.4km
③	ASG	n_L=150, n_R=152	10Ω	CGF	1.2km

fault cable sections and those near the fault in the three cases are illustrated in Fig. 8. In Fig. 8, the legends 'I0(n_L-n_R)' and 'Is(n_L-n_R)' represent the zero-sequence current and grounding line current at the local end of the cable section between nodes N_L and N_R, respectively.

It can be seen that the grounding line current and zero-sequence one varies significantly prior to and after the fault ($t_0 = 0.08$s), which can be used to detect the fault. For the fault cable section, the amplitude of the grounding line current is more than two times of that of the zero-sequence current. For the healthy cable section, the amplitude of the grounding line current is about three times of that of the zero-sequence current. The results shown by Fig. 8 are consistent with the theoretical analysis shown in eq. (5) and eq. (6). Due to space limitation, the space-measurement matrix $\boldsymbol{M}_{\rm sm}$ and the vector $\boldsymbol{V}_s$ determined by the amplitude difference ratio matrix $\boldsymbol{M}_r$ for each case are expressed by bar graphs, as shown in Fig. 9. m_{gh} and v_u on the ordinate represent the element in $\boldsymbol{M}_{\rm sm}$ and $\boldsymbol{V}_{\rm s}$. The node numbers in Fig. 9 (a) corresponding to the actual nodes of the distribution network are listed in Table VI. 'NN' represents the node number.

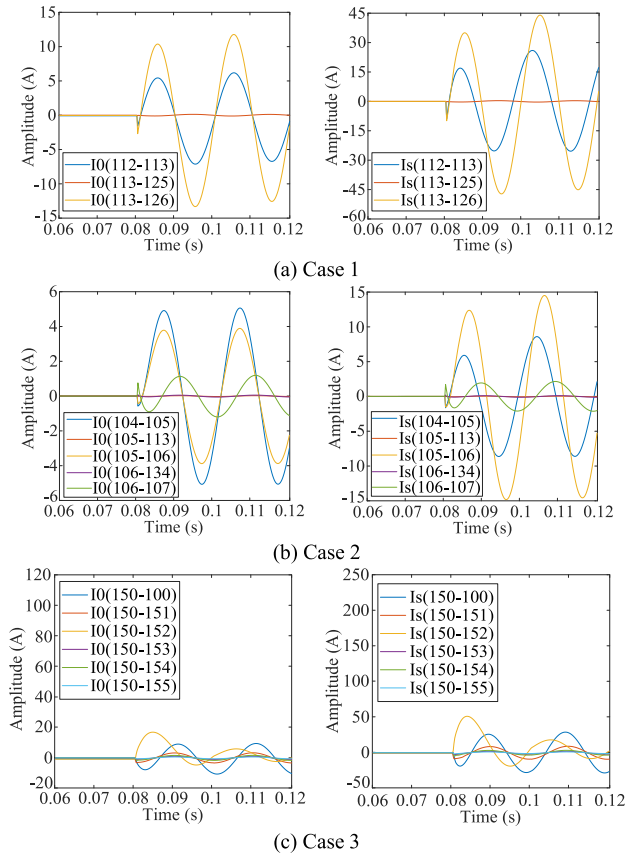

Fig. 8. The grounding line currents and zero-sequence ones at the local ends of the cable feeders and sections near the fault.

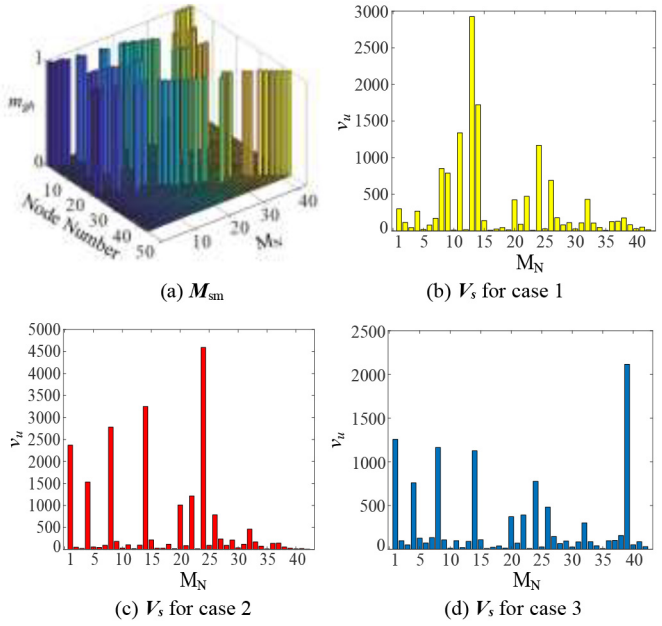

Fig. 9. The space-measurement matrix $\boldsymbol{M}_{\mathrm{sm}}$ and the vector $\boldsymbol{V}_{\mathrm{s}}$ determined by the amplitude difference ratio matrix $\boldsymbol{M}_{\mathrm{r}}$ for each case.

The fault section identification results of the three cases are listed in Table VII. It can be observed that the determined numbers of the local and remote ends of the fault cable sections are identical to those preset in the fault simulations. The results verify the effectiveness of the proposed fault section identification method.

TABLE VI
NODE NUMBER CORRESPONDING TO THE ACTUAL NODE

Node	NN	Node	NN	Node	NN	Node	NN	Node	NN
150	1	100	2	101	3	102	4	103	5
104	6	105	7	106	8	107	9	108	10
109	11	111	12	112	13	113	14	114	15
115	16	116	17	117	18	121	19	122	20
123	21	124	22	125	23	126	24	127	25
128	26	129	27	130	28	131	29	132	30
133	31	134	32	135	33	136	34	137	35
138	36	139	37	140	38	151	39	152	40
153	41	154	42	155	43	---	---	---	---

TABLE VII
FAULT SECTION IDENTIFICATION RESULTS

Case	ζ_{max}	$\lvert i_{SL\_MF}(t)\rvert$	$u_{\max}$	$\boldsymbol{M}_{sm}(n_L,u_{\max})$=1	$\boldsymbol{M}_{sm}(n_R,u_{\max})$=1
①	0.1A	$>\zeta_{max}$	13	$n_L=113$	$n_R=126$
②			24	$n_L=105$	$n_R=106$
③			39	$n_L=150$	$n_R=152$

TABLE VIII
DETAILS OF THE GROUND SYSTEM WITH DIFFERENT FAULT CONDITIONS

FCS	NG	R_F	FT	x_F	N_F
n_L=108, n_R=109	UNG/RG/ ASG	10Ω/200Ω/ 500Ω	CSF/CGF	LE/MP/ RE	54
n_L=102, n_R=103					54
n_L=111, n_R=123					54

B. Sensitivity Analysis

1) Effects of Ground System With Different Fault Conditions: The neutral point at the upstream network are indirectly grounded (using a ground transformer), producing the compensation current. Different ground systems correspond to different compensation currents, which affects the amplitude of the zero-sequence current and grounding line current. There are three main ground system for the distribution network: ungrounded system, arc-suppression coil grounded system, and resistance grounded system. To investigate the effect of the ground system on the fault location, three ground systems are considered in the experiment. In each ground system, 54 different fault experiments are conducted. The details of the conducted fault simulations are displayed in Table VIII. In the table, 'GS' represents the ground system. 'UNG', 'ASG', and 'RG' denote the ungrounded system, arc-suppression coil grounded system, and resistance grounded system, respectively. 'FCS' represents the fault cable section. 'NF' denotes the total number of the simulated faults in each neutral grounding mode. 'LE' and 'RE' represent the faults are 0.1km away from the local and remote ends of the cable section, respectively. 'MP' denotes that the fault is located at the middle point of the cable section. Fig. 10 displays the amplitude differences between the grounding line currents and zero-sequence ones of the fault

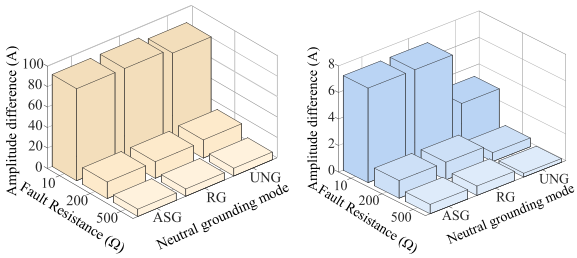

(a) Fault cable (b) Healthy cable

Fig. 10. Amplitude differences between the grounding line and zero-sequence currents in different ground system with different fault resistances.

TABLE IX
FAULT SECTION IDENTIFICATION RESULTS

FCS	ζ_{max}	$\lvert i_{SL\_MF}(t)\rvert$	$u_{\max}$	C_{FSI}
n_L=108, n_R=109			36	100%
n_L=102, n_R=103	0.1A	$>\zeta_{max}$	14	100%
n_L=111, n_R=123			6	100%

TABLE X
FAULT CASES WITH DIFFERENT DG PENETRATION LEVELS

Case	DG penetration level	NG	FCS	x_F
①	High Low	UNG	n_L=107, n_R=115	2.8km
②	High Low	RG	n_L=105, n_R=106	1.2km
③	High Low	ASG	n_L=116, n_R=135	0.2km

and healthy cables in different ground systems. The fault is located in the cable section between nodes 108 and 109. The amplitude difference varies with the ground system type and fault resistances. In general, the amplitude difference is more significant in the resistance grounded system than that in the ungrounded system. The fault section identification results are summarized in Table IX. 'C_{FSI}' represents the accuracy of fault section identification. It can be concluded from the results that the ground system with different fault conditions has little impact on the fault location.

2) Effects of DG Penetration Levels: To test the performance of the method with DG, different DG penetration levels are considered in the fault simulation. Table X lists the fault cases with DG at high and low penetration levels. In the cases, the CGFs with 200Ω are simulated at different locations of the fault cable sections. In the table, the high and low DG penetration levels mean 70% and 10% of the total loads are fed by DG1, DG2, and DG3. The zero-sequence currents and grounding line ones of the fault cable sections and those near the fault in case ② are depicted in Fig. 11. It can be seen that the amplitudes of the zero-sequence currents and grounding line currents with high DG penetration level are nearly identical to those with low DG penetration level. The fault section identification results are displayed in Table XI. It can be concluded that the method is barely affected by DG penetration level.

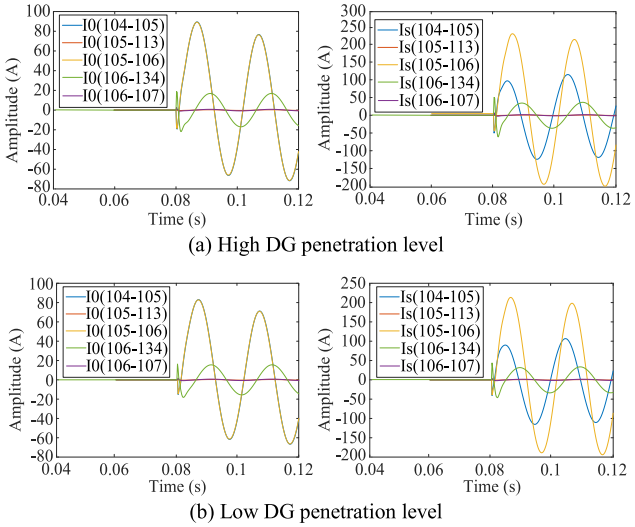

(a) High DG penetration level

(b) Low DG penetration level

Fig. 11. The grounding line currents and zero-sequence ones of the cable feeders and sections near the fault in case ②.

TABLE XI
FAULT SECTION IDENTIFICATION RESULTS WITH DIFFERENT DG PENETRATION LEVELS

Case	ζ_{max}	$\lvert i_{SL\_MF}(t)\rvert$	$u_{\max}$	$\boldsymbol{M}_{sm}(n_L, u_{\max})$=1	$\boldsymbol{M}_{sm}(n_R, u_{\max})$=1
①			27	n_L = 107	n_R = 115
②	0.1A	$>\zeta_{max}$	24	n_L = 105	n_R = 106
③			30	n_L = 116	n_R = 135

3) Effects of Unbalanced Loads and Laterals: The actual urban distribution networks have many unbalanced loads and laterals. The unbalances only affect the steady-state voltages and currents in the normal operation. Since the proposed method uses the amplitudes of the current signals in the transient time interval after a fault occurs in the cable, the unbalanced loads and laterals have little impact on the method. In order to test the performance of the proposed method with unbalanced loads and different types of laterals, part of the original balanced loads and laterals in the distribution network have been replaced by the unbalanced ones. The unbalanced loads and laterals are listed in Table XII. It can be observed that the loads at the nodes 129, 136 and 140 have been changed to the three-phase unbalanced ones. There are eight laterals and the connected loads have been changed into the single-phase, two-phase, and three-phase unbalanced ones. Three CGFs (fault resistance is 300Ω) are simulated at different locations of the distribution cable network with the unbalanced loads. By using the proposed method, the fault section identification results are presented in Table XIII. It can be seen that the fault section can be correctly identified by the proposed method, demonstrating that the method is not affected by the unbalanced conditions.

4) Effects of Intermittent Faults: The intermittent fault may occur in the distribution cable at the early stage of the fault. Since the proposed method only uses the maximum values of the current signals in time domain, it is not affected by the intermittent faults with varying fault resistances in theory. In

TABLE XII
UNBALANCED LOADS AND LATERALS IN THE SIMULATION MODEL

Node	Load(MW, MVar)	Laterals	Type
121	Phase A 0.25+j0.02 Phase B 0 Phase C 0	100-121	single-phase
124	Phase A 0.26+j0.04 Phase B 0.21+j0.02 Phase C 0	111-124	two-phase
129	Phase A 0.29+j0.02 Phase B 0.23+j0.05 Phase C 0.19+j0.01	114-129	three-phase
131	Phase A 0.3+j0.01 Phase B 0.28+j0.05 Phase C 0	103-131	two-phase
133	Phase A 0.26+j0.03 Phase B 0 Phase C 0	105-133	single-phase
136	Phase A 0.26+j0.04 Phase B 0.11+j0.05 Phase C 0.05+j0.02	116-136	three-phase
138	Phase A 0.28+j0.03 Phase B 0.31+j0.01 Phase C 0	117-138	two-phase
140	Phase A 0.24+j0.05 Phase B 0.32+j0.01 Phase C 0.18+j0.03	108-140	three-phase

TABLE XIII
FAULT SECTION IDENTIFICATION RESULTS OF THE FAULT CASE

FCS	ζ_{max}	$\lvert i_{SL\ MF}(t)\rvert$	$u_{\max}$	$\boldsymbol{M}_{sm}(n_L, u_{\max})=1$	$\boldsymbol{M}_{sm}(n_R, u_{\max})=1$
112-127			11	$n_L = 112$	$n_R = 127$
114-129	0.1A	$> \zeta_{max}$	19	$n_L = 114$	$n_R = 129$
108-140			37	$n_L = 108$	$n_R = 140$

TABLE XIV
FAULT SECTION IDENTIFICATION RESULTS WITH INTERMITTENT FAULTS

FCS	ζ_{max}	$\lvert i_{SL\ MF}(t)\rvert$	$u_{\max}$	$\boldsymbol{M}_{sm}(n_L, u_{\max})=1$	$\boldsymbol{M}_{sm}(n_R, u_{\max})=1$
114-128			21	$n_L = 114$	$n_R = 128$
117-139	0.1A	$> \zeta_{max}$	39	$n_L = 117$	$n_R = 139$
150-155			40	$n_L = 150$	$n_R = 152$

order to test the performance of the method against these types of the faults, the intermittent faults have simulated at different locations in the distribution cable network. Fig. 12 depicts the zero-sequence and grounding line currents at the local end of the fault and healthy cables. I_0 and I_S in the legend represent the zero-sequence current and the grounding line current. It can be observed that these current signals distort significantly. There exist many times of burning and extinguishing of the arc. In Fig. 12(a), the maximum values of the grounding line and zero-sequence currents reach about 175A and 50A, respectively. In Fig. 12(b), these values are close to 20A and 5A. Thus, the difference between the maximum values of the grounding line and zero-sequence currents in the fault cable is far larger than that in the healthy cable. The fault cable can be still identified by using the proposed method. The detailed fault section identification results with intermittent faults are lusted in Table XIV. It can be seen that the proposed method can correctly identify the fault cable in these faults, verifying that the method is not affected by the intermittent faults.

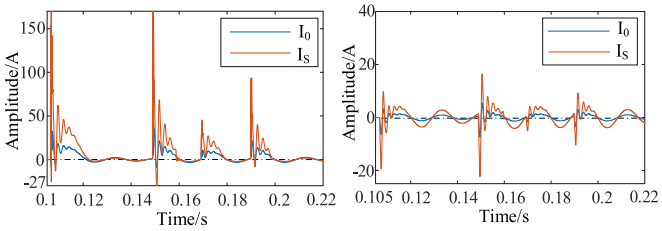

(a) Currents of the fault cable (b) Currents of the healthy cable

Fig. 12. Zero-sequence and grounding line currents of the fault and healthy cables with intermittent faults.

TABLE XV
COMPARISON RESULTS WITH SEVERAL METHODS

Method	Signal	TC	SY	PK	f_S	T_C
[5]	I_P	NC	√	√	25kHz	0.6s
[8]	U_p	NC	√	√	5kHz	0.2s
[13]	I_p, I_0	NC	√	√	7.68kHz	3s
[26]	I_S	TCS	×	×	3.2kHz	0.5s
[28]	U_0	NC	××	√	50kHz	1s
Proposed Method	I_S, I_0	TCSA	××	×	3.2kHz	0.02s

C. Comparison Work

A comparative study between the proposed method and several other ones is conducted. The comparison of these methods is based on the same simulation test system in Fig. 6. The simulations and calculations are all performed in a computer whose processor is Intel Core i5-6300HQ @ 2.3GHz. The results are listed in Table XV. 'TC' represents the three-core cable multi-conductor structure. 'SY' represents the time synchronization. 'PK' denotes the prior knowledge. f_S is the sampling rate. T_C represents the computation time. I_p and U_p represent the phase current and voltage signals. I_0, U_0 and I_S denote the zero-sequence current, zero-mode voltage and grounding line current. 'NC' means the method does not consider TC. 'TCS' represents the multi-conductor model considering the three-phase core conductors and sheath. 'TCSA' represents the multi-conductor model considering the three-phase core conductors, sheath and armor. Symbol '✓' represents the item is required. Symbols '×' and '××' mean that the strict time synchronization is not required and that the time synchronization is totally not required.

Only the proposed algorithm uses both the grounding line current and zero-sequence current. Compared with the phase voltages, currents, or zero-sequence components used in the other methods, it's easier to measure the grounding line current and zero-sequence current at the local end of the cable. Only the proposed method considers the complete conductor structure of a real distribution cable. Only the proposed method and the one in [28] do not require time synchronization in the slightest. All the methods except the proposed method and that in [26] need prior knowledge. The proposed method requires a low sampling rate. Additionally, the computing time of the proposed method is only 0.02s which is far shorter than those of the other methods. It can be seen that the proposed method has more advantages over the current ones.

IV. Conclusion

For the urban distribution cable network, this paper proposes a novel method to identify the fault section. The grounding line currents and zero-sequence ones at the local end of the cable sections, acquired by current measurement units, are employed to conduct the fault detection and fault section location. General conclusions are as follows.

First, after a fault occurs in the distribution cable, the grounding line current at the local end of a distribution three-core cable in healthy cable section is larger than the zero-sequence current. In detail, the amplitude of the grounding line current at the local end is smaller than three times the one of the zero-sequence current.

Second, after a fault occurs in a cable section, both the grounding line current and zero-sequence current increase significantly. The grounding line current at the local end of the fault cable section is also larger than the zero-sequence current. The grounding line current at the local end is at least three times as large as the zero-sequence current.

Third, the amplitude difference between the grounding line current and zero-sequence current at the local end of the fault cable section is larger than that of any healthy cable section. Combining the distribution network topology, locations of the measurement units and amplitude differences, the fault cable section can be accurately and quickly identified by the proposed method.

Fourth, the proposed method is verified by simulation to be robust to different conditions including the fault resistance, fault location, and neutral grounding mode. It is also applicable to the distribution network with DGs.

Appendix A

According to the created circuit model in normal operation in Fig. 2(a), the currents flowing through the self-impedance of the three-phase core conductors, metallic sheath and armor are presented by using the electrical quantities at the local end of the healthy cable *k:*

$$\begin{cases} I_{AA} = I_{AL} - Y_{ASl}(U_{AL} - U_{SL}) \\ I_{BB} = I_{BL} - Y_{BSl}(U_{BL} - U_{SL}) \\ I_{CC} = I_{CL} - Y_{CSl}(U_{CL} - U_{SL}) \\ (1 + Y_{MMl}R_{SG})I_{SLk} + I_{SS} + I_{MM} = 3Y_{ASl}(U_{0Lk} - U_{SL}) \end{cases} \tag{A1}$$

where I_{PP}, I_{SS} and I_{MM} represent the currents flowing through the self-impedances of the core conductor in phase P, metallic sheath, and armor of cable k, respectively. I_{PL} and I_{SLk} denote the currents of the core conductor in phase P and grounding line at the local end of cable k. U_{PL} and U_{SL} are the voltages to ground of the core conductor in phase P and metallic sheath at the local end. U_{0Lk} represents the zero-sequence voltage at the local end.

Similarly, the currents flowing through the self-impedance of the three-phase core conductors, metallic sheath and armor of the cable in normal operation can be also expressed by the electrical quantities at the remote end:

$$\begin{cases} I_{AA} = I_{AR} + Y_{ASl}(U_{AR} - U_{SR}) \\ I_{BB} = I_{BR} + Y_{BSl}(U_{BR} - U_{SR}) \\ I_{CC} = I_{CR} + Y_{CSl}(U_{CR} - U_{SR}) \\ (1 + Y_{MMl}R_{SG})I_{SRk} = I_{MM} + I_{SS} + 3Y_{ASl}(U_{0Rk} - U_{SR}) \end{cases} \tag{A2}$$

In (A2), I_{PR} and I_{SRk} denote the currents of the core conductor in phase P and grounding line at the remote end of cable k. Since I_{SRk} is far less than I_{SLk}, I_{SRk} can be negligible in analysis. U_{PR} and U_{SR} are the voltages to ground of the core conductor in phase P and metallic sheath at the remote end. U_{0Rk}represents the zero-sequence voltage at the remote end.

By integrating (A1) and (A2), we have

$$\begin{cases} I_{0Lk} - I_{0Rk} = Y_{ASl}((U_{0Rk} - U_{SR}) + (U_{0Lk} - U_{SL})) \\ \frac{1}{3}(1 + Y_{MMl}R_{SG})(I_{SLk} + I_{SRk}) = Y_{ASl}((U_{0Lk} - U_{SL}) + (U_{0Rk} - U_{SR})) \end{cases} \tag{A3}$$

where I_{0Lk} and I_{0Rk} represent the zero-sequence currents at the local and remote end of cable k. After the single-phase fault occurs in the cable, $I_{0Rk} \approx 0$ and $I_{0Rk} \approx 0$. Simplifying (A3), the following expression can be obtained:

$$I_{0Lk} = \frac{1}{3}I_{SLk}(1 + Y_{MMl}R_{SG}) \tag{A4}$$

The relationship between the grounding line current and zero-sequence current at the local end of the healthy cable k can be formulated by

$$|1 + Y_{MMl}R_{SG}||I_{SLk}| = 3|I_{0Lk}| \tag{A5}$$

Appendix B

Based on the model in Fig. 2(b), the currents at the local end of the fault cable j can be presented by

$$\begin{cases} I_{ALf} = I_{AAL} + Y_{ASL}\left(U_{ALf} - U_{SLf}\right) \\ I_{BLf} = I_{BBL} + Y_{BSL}\left(U_{BLf} - U_{SLf}\right) \\ I_{CLf} = I_{CCL} + Y_{CSL}\left(U_{CLf} - U_{SLf}\right) \\ I_{SSL} + I_{MML} + (1 + Y_{MML}R_{SG})I_{SLj} = 3Y_{ASL}\left(U_{0Lj} - U_{SLf}\right) \end{cases} \tag{B1}$$

In (B1), I_{PPL}, I_{SSL} and I_{MML} represent the currents flowing through the self-impedances of the core conductor in phase P, metallic sheath, and armor of cable j upstream the fault, respectively. I_{PLf} and I_{SLj} denote the currents of the core conductor in phase P and grounding line at the local end of cable j. U_{PLf} and U_{SLf} are the voltages to ground of the core conductor in phase P and metallic sheath at the local end of cable j. U_{0Lj} represents the zero-sequence voltage at the local end of cable j.

The voltages across the self-impedances of the core conductor in phase P, metallic sheath, and armor of cable j upstream the fault are expressed by

$$\begin{bmatrix} U_{AAL} \\ U_{BBL} \\ U_{CCL} \\ U_{SSL} \\ U_{MML} \end{bmatrix} = \begin{bmatrix} Z_{AAL} & Z_{ABL} & Z_{ACL} & Z_{ASL} & Z_{AML} \\ Z_{ABL} & Z_{BBL} & Z_{BCL} & Z_{BSL} & Z_{BML} \\ Z_{ACL} & Z_{BCL} & Z_{CCL} & Z_{CSL} & Z_{CML} \\ Z_{ASL} & Z_{BSL} & Z_{CSL} & Z_{SSL} & Z_{SML} \\ Z_{AML} & Z_{BML} & Z_{CML} & Z_{SML} & Z_{MML} \end{bmatrix} \cdot \begin{bmatrix} I_{AAL} \\ I_{BBL} \\ I_{CCL} \\ I_{SSL} \\ I_{MML} \end{bmatrix} \tag{B2}$$

where U_{PPL}, U_{SSL} and U_{MML} denote the voltages across the self-impedances of the core conductor in phase P, metallic sheath, and armor of cable j upstream the fault, respectively. I_{SSL} and I_{MML} represent the currents flowing through the metallic sheath and armor of cable j upstream the fault, respectively. I_{SLj} represents the grounding line current at the local end of cable j. I_{SG}, I_{MSG} and I_{MG} denote the ground currents generated by Y_{SSL}, Y_{SML} and Y_{MML} of cable j.

Considering the arc fault model [29] and using the voltages to ground at the local end, those of the core conductor in phase P, metallic sheath, and armor of cable j at the fault point can be estimated by

$$\begin{cases} U_{FAGL} = U_{ALf} - U_{AAL}, U_{FBGL} = U_{BLf} - U_{BBL} \\ U_{FCGL} = U_{CLf} - U_{CCL}, U_{FSGL} = U_{SLf} - U_{SSL} \\ U_{FMGL} = R_{SG} I_{SLj} - U_{MML} \\ \frac{d(R_{fw}(t)^{-1})}{dt} = \frac{L_w}{\alpha \max(I_{fw})} \left(\frac{|I_{fw}|}{V_d L_w} - \frac{1}{R_{fw}(t)} \right), w \in \{1, 2, 3\} \end{cases} \tag{B3}$$

where U_{FPGL}, U_{FSGL} and U_{FMGL} are the voltages to ground of the core conductor in phase P, metallic sheath, and armor of cable j at the fault point derived by those at the remote end. $R_{fw}(t)$ ($w \in \{1, 2, 3\}$) represents the arc fault resistance varying with time shown in Fig. 2. L_w denotes the length of the arc fault. α is the empirical coefficient. I_{fw} represents the peak of the arc current. V_d denotes the voltage drop in per unit length of the arc. According to Fig. 2, it is easy to know that

$$\begin{cases} U_{FCGL} - U_{FSGL} = R_{f1}(t) I_{f1} \\ U_{FCGL} - U_{FMGL} = R_{f2}(t) I_{f2} \\ U_{FMGL} = R_{f3}(t) I_{f3} \end{cases} \tag{B4}$$

Similarly, the currents at the remote end of the fault cable j can be shown by

$$\begin{cases} I_{ARf} = I_{AAR} - Y_{ASR}(U_{ARf} - U_{SRf}) \\ I_{BRf} = I_{BBR} - Y_{BSR}(U_{BRf} - U_{SRf}) \\ I_{CRf} = I_{CCR} - Y_{CSR}(U_{CRf} - U_{SRf}) \\ I_{SSR} + I_{MMR} + 3Y_{ASR}(U_{0Rj} - U_{SRf}) = (1 + Y_{MMR} R_{SG}) I_{SRj} \end{cases} \tag{B5}$$

In (B5), I_{PPR}, I_{SSR} and I_{MMR} represent the currents flowing through the self-impedances of the core conductor in phase P, metallic sheath, and armor of cable j downstream the fault, respectively. I_{PRf} and I_{SRj} denote the currents of the core conductor in phase P and grounding line at the remote end. U_{PRf} and U_{SRf} are the voltages to ground of the core conductor in phase P and metallic sheath at the remote end. U_{0Rj} represents the zero-sequence voltage at the remote end.

The voltages across the self-impedances of the core conductor in phase P, metallic sheath, and armor of cable j downstream the fault are computed as

$$\begin{bmatrix} U_{AAR} \\ U_{BBR} \\ U_{CCR} \\ U_{SSR} \\ U_{MMR} \end{bmatrix} = \begin{bmatrix} Z_{AAR} & Z_{ABR} & Z_{ACR} & Z_{ASR} & Z_{AMR} \\ Z_{ABR} & Z_{BBR} & Z_{BCR} & Z_{BSR} & Z_{BMR} \\ Z_{ACR} & Z_{BCR} & Z_{CCR} & Z_{CSR} & Z_{CMR} \\ Z_{ASR} & Z_{BSR} & Z_{CSR} & Z_{SSR} & Z_{SMR} \\ Z_{AMR} & Z_{BMR} & Z_{CMR} & Z_{SMR} & Z_{MMR} \end{bmatrix} \cdot \begin{bmatrix} I_{AAR} \\ I_{BBR} \\ I_{CCR} \\ I_{SSR} \\ I_{MMR} \end{bmatrix} \tag{B6}$$

In (B6), U_{PPR}, U_{SSR} and U_{MMR} represent the voltages across the self-impedances of the core conductor in phase P, metallic sheath, and armor of cable j downstream the fault, respectively. Using the voltages to ground at the remote end, those of the core conductor in phase P, metallic sheath, and armor of cable j at the fault point can be also estimated by

$$\begin{cases} U_{FAGR} = U_{ARf} + U_{AAR}, U_{FBGR} = U_{BRf} + U_{BBR} \\ U_{FCGR} = U_{CRf} + U_{CCR}, U_{FSGR} = U_{SRf} + U_{SSR} \\ U_{FMGR} = R_{SG} I_{SRj} + U_{MMR} \end{cases} \tag{B7}$$

where U_{FPGR}, U_{FSGR} and U_{FMGR} are the voltages to ground of the core conductor in phase P, metallic sheath, and armor of cable j at the fault point derived by those at the remote end.

Similarly, we can obtain that

$$\begin{cases} U_{FCGR} - U_{FSGR} = R_{f1}(t) I_{f1} \\ U_{FCGR} - U_{FMGR} = R_{f2}(t) I_{f2} \\ U_{FMGR} = R_{f3}(t) I_{f3} \end{cases} \tag{B8}$$

According to (B4) and (B8), we have

$$\begin{cases} U_{FAGR} = U_{FAGL}, U_{FBGR} = U_{FBGL}, U_{FCGR} = U_{FCGL}, \\ U_{FSGR} = U_{FSGL}, U_{FMGR} = U_{FMGL} \end{cases} \tag{B9}$$

By Integrating (B1)-(B2), we have

$$\begin{cases} 3I_{0Lj} = \sum_{P \in \{A,B,C\}} I_{PPL} + 3Y_{ASL}(U_{0Lj} - U_{SLf}) \\ 3Y_{ASL} U_{SLf} + (1 + Y_{MML} R_{SG}) I_{SLj} + (I_{SSL} + I_{MML}) = 3Y_{ASL} U_{0Lj} \\ \sum_{P \in \{A,B,C\}} I_{PPL} = \sum_{i=1}^{3} \boldsymbol{Z}_L^{-1} \boldsymbol{U}_{PPL}\{i\} \\ \boldsymbol{Z}_L = \begin{bmatrix} Z_{AAL} & Z_{ABL} & Z_{ACL} & Z_{ASL} & Z_{AML} \\ Z_{BAL} & Z_{BBL} & Z_{BCL} & Z_{BSL} & Z_{BML} \\ Z_{CAL} & Z_{CBL} & Z_{CCL} & Z_{CSL} & Z_{CML} \\ Z_{SAL} & Z_{SBL} & Z_{SCL} & Z_{SSL} & Z_{SML} \\ Z_{MAL} & Z_{MBL} & Z_{MCL} & Z_{MSL} & Z_{MML} \end{bmatrix}, \boldsymbol{U}_{PPL} = \begin{bmatrix} U_{AAL} \\ U_{BBL} \\ U_{CCL} \\ U_{SSL} \\ U_{MML} \end{bmatrix} \end{cases} \tag{B10}$$

Similarly, based on (B5)-(B6), we have

$$\begin{cases} 3I_{0Rj} = \sum_{P \in \{A,B,C\}} I_{PPR} - 3Y_{ASR}(U_{0Rj} + U_{SRf}) \\ 3Y_{ASR} U_{SRf} + (1 + Y_{MMR} R_{SG}) I_{SRj} - (I_{SSR} + I_{MMR}) = 3Y_{ASR} U_{0Rj} \\ \sum_{P \in \{A,B,C\}} I_{PPR} = \sum_{i=1}^{3} \boldsymbol{Z}_R^{-1} \boldsymbol{U}_{PPR}\{i\} \\ \boldsymbol{Z}_R = \begin{bmatrix} Z_{AAR} & Z_{ABR} & Z_{ACR} & Z_{ASR} & Z_{AMR} \\ Z_{BAR} & Z_{BBR} & Z_{BCR} & Z_{BSR} & Z_{BMR} \\ Z_{CAR} & Z_{CBR} & Z_{CCR} & Z_{CSR} & Z_{CMR} \\ Z_{SAR} & Z_{SBR} & Z_{SCR} & Z_{SSR} & Z_{SMR} \\ Z_{MAR} & Z_{MBR} & Z_{MCR} & Z_{MSR} & Z_{MMR} \end{bmatrix}, \boldsymbol{U}_{PPR} = \begin{bmatrix} U_{AAR} \\ U_{BBR} \\ U_{CCR} \\ U_{SSR} \\ U_{MMR} \end{bmatrix} \end{cases} \tag{B11}$$

Based on (B10)-(B11), the following expressions can be acquired:

$$\begin{cases} 3(I_{0Lj} + I_{0Rj}) = \sum_{i=1}^{3} \boldsymbol{Z}_L^{-1} \boldsymbol{U}_{PPL}\{i\} + \sum_{i=1}^{3} \boldsymbol{Z}_R^{-1} \boldsymbol{U}_{PPR}\{i\} + \\ 3(Y_{ASL} U_{0Lj} - Y_{ASR} U_{0Rj} + Y_{ASR} U_{SR} - Y_{ASL} U_{SL}) \\ 3Y_{ASR} U_{SR} - 3Y_{ASL} U_{SL} + (1 + Y_{MMR} R_{SG}) I_{SRj} - (1 + Y_{MML} R_{SG}) I_{SLj} \\ -(I_{SSL} + I_{SSR} + I_{MML} + I_{MMR}) = 3(Y_{ASR} U_{0Rj} - Y_{ASL} U_{0Lj}) \end{cases} \tag{B12}$$

Integrating (B3) and (B9), we can obtain that

$$\boldsymbol{U}_L - \boldsymbol{U}_R = \boldsymbol{U}_{PPL} + \boldsymbol{U}_{PPR}, \boldsymbol{U}_L = \begin{bmatrix} U_{ALf} \\ U_{BLf} \\ U_{CLf} \\ U_{SLf} \\ R_{SG} I_{SLj} \end{bmatrix}, \boldsymbol{U}_R = \begin{bmatrix} U_{ARf} \\ U_{BRf} \\ U_{CRf} \\ U_{SRf} \\ R_{SG} I_{SRj} \end{bmatrix} \tag{B13}$$

Simplifying (B12) and integrating with (B13), we have

$$\begin{cases} |3I_{0Lj}| \le |(F_1 + G_1 + F_2 + G_2)| + |I_{SLj}| \\ |F_1| = \left| \sum_{i=1}^{5} \boldsymbol{Z}^{-1} \boldsymbol{U}_{PPL}\{i\} \right| < \sum_{i=1}^{5} |\boldsymbol{Z}^{-1} \boldsymbol{U}_L|\{i\}|F_2| \\ \quad = \left| \sum_{i=4}^{5} \boldsymbol{Z}^{-1} \boldsymbol{U}_{PPL}\{i\} \right| < \sum_{i=4}^{5} |\boldsymbol{Z}^{-1} \boldsymbol{U}_L|\{i\} \\ |G_1| = \left| \sum_{i=1}^{5} \boldsymbol{Z}^{-1} (\boldsymbol{U}_L - \boldsymbol{U}_R)\{i\} \right|, |G_2| = \left| \sum_{i=4}^{5} \boldsymbol{Z}^{-1} (\boldsymbol{U}_L - \boldsymbol{U}_R)\{i\} \right| \end{cases} \tag{B14}$$

In (B14), $\boldsymbol{Z}^{-1}\boldsymbol{U}_L$ is on the order of 10^{-5}. Ignoring the small items in (B14), we have

$$\left|3I_{0Lj}\right| \le |(2G_1 + G_2)| + \left|I_{SLj}\right| \tag{B15}$$

Expanding (B15), we can obtain

$$3\left|I_{0Lj}\right| \le \left|3R_{SG}\sum_{i=5,j=1}^{j=5}\boldsymbol{Z}^{-1}(i,j) + 1\right| + \left|I_{SLj}\right| \tag{B16}$$

In (B16), $\sum|\boldsymbol{Z}^{-1}|$ is on the order of 10^{-3}. It can be inferred that

$$3\left|I_{0Lj}\right| \le \left|I_{SLj}\right| \tag{B17}$$

REFERENCES

[1] B. Chen, N. Yu, B. Chen, C. Tian, Y. Chen, and G. Chen, "Fault location for underground cables in ungrounded MV distribution networks based on ZSC signal injection," *IEEE Trans. Power Del.*, vol. 36, no. 5, pp. 2965–2977, Oct. 2021.

[2] D. Xiao, T. He, R. Xiao, and X. Du, "Segment location for single-phase-to-ground fault in neutral non-effectively grounded system based on distributed electric-field measurement," *Electr. Power Syst. Res.*, vol. 184, Jul. 2020, Art. no. 106321.

[3] A. A. P. Bíscaro, R. A. F. Pereira, M. Kezunovic, and J. R. S. Mantovani, "Integrated fault location and power-quality analysis in electric power distribution systems," *IEEE Trans. Power Del.*, vol. 31, no. 2, pp. 428–436, Apr. 2016.

[4] M. A. Barik, A. Gargoom, M. A. Mahmud, M. E. Haque, H. Al-Khalidi, and A. M. T. Oo, "A decentralized fault detection technique for detecting single phase to ground faults in power distribution systems with resonant grounding," *IEEE Trans. Power Del.*, vol. 33, no. 5, pp. 2462–2473, Oct. 2018.

[5] M. Daisy and R. Dashti, "Single phase fault location in electrical distribution feeder using hybrid method," *Energy*, vol. 103, pp. 356–368, May 2016.

[6] J. Li, M. Gao, B. Liu, F. Gao, and J. Chen, "Fault location algorithm in distribution networks considering distributed capacitive current," *IEEE Trans. Power Del.*, vol. 36, no. 5, pp. 2785–2793, Oct. 2021.

[7] X. Shi, R. Qiu, Z. Ling, F. Yang, H. Yang, and X. He, "Spatio-temporal correlation analysis of online monitoring data for anomaly detection and location in distribution networks," *IEEE Trans. Smart Grid*, vol. 11, no. 2, pp. 995–1006, Mar. 2020.

[8] R. Dashti and J. Sadeh, "Fault section estimation in power distribution network using impedance-based fault distance calculation and frequency spectrum analysis," *IET Gener. Transm. Distrib.*, vol. 8, no. 8, pp. 1406–1417, Jan. 2014.

[9] W. C. Santos, F. V. Lopes, N. S. D. Brito, and B. A. Souza, "High-impedance fault identification on distribution networks," *IEEE Trans. Power Del.*, vol. 32, no. 1, pp. 23–32, Feb. 2017.

[10] X. Wang, J. Gao, M. Chen, X. Wei, Y. Wei, and Z. Zeng, "Faulty line detection method based on optimized bistable system for distribution network," *IEEE Trans. Ind. Informat.*, vol. 14, no. 4, pp. 1370–1381, Apr. 2018.

[11] X. Wei, X. Wang, J. Gao, D. Yang, K. Wei, and L. Guo, "Faulty feeder detection for single-phase-to-ground fault in distribution networks based on transient energy and cosine similarity," *IEEE Trans. Power Del.*, vol. 37, no. 5, pp. 3968–3979, Oct. 2022.

[12] X. Wang et al., "Location of single phase to ground faults in distribution networks based on synchronous transients energy analysis," *IEEE Trans. Smart Grid*, vol. 11, no. 1, pp. 774–785, Jan. 2020.

[13] F. V. Lopes et al., "Practical methodology for two-terminal traveling wave-based fault location eliminating the need for line parameters and time synchronization," *IEEE Trans. Power Del.*, vol. 34, no. 6, pp. 2123–2134, Dec. 2019.

[14] L. Xie, L. Luo, Y. Li, Y. Zhang, and Y. Cao, "A traveling wave-based fault location method employing VMD-TEO for distribution network," *IEEE Trans. Power Del.*, vol. 12, no. 4, pp. 1987–1998, Aug. 2020.

[15] S. Shi, B. Zhu, A. Lei, and X. Dong, "Fault location for radial distribution network via topology and reclosure-generating traveling waves," *IEEE Trans. Smart Grid*, vol. 10, no. 6, pp. 6404–6413, Nov. 2019.

[16] H. Shu, X. Liu, and X. Tian, "Single-ended fault location for hybrid feeders based on characteristic distribution of traveling wave along a line," *IEEE Trans. Power Del.*, vol. 36, no. 1, pp. 339–349, Feb. 2021.

[17] A. C. Adewole, R. Tzoneva, and S. Behardien, "Distribution network fault section identification and fault location using wavelet entropy and neural networks," *Appl. Soft Comput.*, vol. 46, pp. 296–306, Sep. 2016.

[18] M.-F. Guo, X.-D. Zeng, D.-Y. Chen, and N.-C. Yang, "Deep-learning-based earth fault detection using continuous wavelet transform and convolutional neural network in resonant grounding distribution systems," *IEEE Sensors J.*, vol. 18, no. 3, pp. 1291–1300, Feb. 2018.

[19] M.-F. Guo, J.-H. Gao, X. Shao, and D.-Y. Chen, "Location of single-line-to-ground fault using 1-d convolutional neural network and waveform concatenation in resonant grounding distribution systems," *IEEE Trans. Instrum. Meas.*, vol. 70, pp. 1–9, 2021, doi: 10.1109/TIM.2020.3014006.

[20] K. Jia, B. Yang, X. Dong, T. Feng, T. Bi, and D. W. P. Thomas, "Sparse voltage measurement-based fault location using intelligent electronic devices," *IEEE Trans. Smart Grid*, vol. 11, no. 1, pp. 48–60, Jan. 2020.

[21] J. Li, Y. Liu, C. Li, D. Zeng, H. Li, and G. Wang, "An FTU-based method for locating single-phase high-impedance faults using transient zero-sequence admittance in resonant grounding systems," *IEEE Trans. Power Del.*, vol. 37, no. 2, pp. 913–922, Apr. 2022.

[22] K. Jiang, H. Wang, M. Shahidehpour, and B. He, "Block-sparse Bayesian learning method for fault location in active distribution networks with limited synchronized measurements," *IEEE Trans. Power Syst.*, vol. 36, no. 4, pp. 3189–3203, Jul. 2021.

[23] Y. Zhang, J. Wang, and M. E. Khodayar, "Graph-based faulted line identification using micro-PMU data in distribution systems," *IEEE Trans. Smart Grid*, vol. 11, no. 5, pp. 3982–3992, Sep. 2020.

[24] Y. Jiang, "Data-driven fault location of electric power distribution systems with distributed generation," *IEEE Trans. Smart Grid*, vol. 11, no. 1, pp. 129–137, Jan. 2020.

[25] I. Kiaei and S. Lotfifard, "Fault section identification in smart distribution systems using multi-source data based on fuzzy petri nets," *IEEE Trans. Smart Grid*, vol. 11, no. 1, pp. 74–83, Jan. 2020.

[26] N. Peng et al., "Edge computing based fault sensing of the distribution cables based on time-domain analysis of grounding line current signals," *IEEE Trans. Power Del.*, vol. 37, no. 5, pp. 4404–4417, Oct. 2022.

[27] P. Zhang, L. Kong, R. Liang, B. Xu, and N. Peng, "Fault location method for three-core cable using amplitude ratio of shield-grounding wire currents," *IEEE Trans. Ind. Informat.*, early access, Jul. 28, 2022, doi: 10.1109/TII.2022.3194626.

[28] N. Peng et al., "Single-phase-to-earth faulty feeder detection in power distribution network based on amplitude ratio of zero-mode transients," *IEEE Access*, vol. 7, pp. 117678–117691, 2019.

[29] W. Zhang, Y. Jing, and X. Xiao, "Model-based general arcing fault detection in medium-voltage distribution lines," *IEEE Trans. Power Del.*, vol. 31, no. 5, pp. 2231–2241, Oct. 2016.